AIAA JOURNAL
Vol. 61, No. 6, June 2023

# Thermomechanical Real-Time Hybrid Simulation: Conceptual Framework and Control Requirements

Herta Montoya,* Shirley J. Dyke,† and Christian E. Silva‡
*Purdue University, West Lafayette, Indiana 47906*
Amin Maghareh§
*Verus Research, Albuquerque, New Mexico 87110*
and
Jaewon Park¶ and Davide Ziviani**
*Purdue University, West Lafayette, Indiana 47906*

https://doi.org/10.2514/1.J062857

**Real-time hybrid simulation (RTHS) is an enabling technology that has transformed engineering experimentation and helped researchers expand modeling capabilities. However, breakthroughs are necessary to expand the range of hybrid simulation methods and, thus, enable experiments with loading conditions representing multiple hazards. This paper discusses the development of a new thermomechanical RTHS framework and a systematic approach to determining RTHS control requirements. First, the framework is established using a representative finite element model of a layered structural system subjected to thermal loading. A complete two-layer system model serves as the reference system, and it is then partitioned into a numerical layer and an experimental layer that share interface conditions. Next, a thermal actuator is introduced to impose dynamic thermal loading on the experimental subsystem, serving as a transfer system. Finally, control and performance metrics are defined to evaluate the realization of interface boundary conditions and map this to the RTHS execution. Through an illustrative example considering the influence of temperature on a lunar habitat, we demonstrate how to establish controller requirements for RTHS and demonstrate that this approach can be used to conduct RTHS on structures with thermomechanical loading.**

Downloaded by NASA LANGLEY RESEARCH CENTER on November 13, 2023 | http://arc.aiaa.org | DOI: 10.2514/1.J062857

## I. Introduction

REAL-TIME hybrid simulation (RTHS) is a cyber-physical testing technique that enabled efficient and cost-effective dynamic testing to evaluate the seismic performance of structural systems [1–6]. This method is especially useful when the full experiment is just not possible in a laboratory due to the size of the full structure or the extreme conditions that must be realized. This class of testing methods has been extended in recent years to enable researchers to conduct realistic experiments to consider multiple hazards and physics [7–10]. A reference system is partitioned into two subsystems: experimental and numerical. The substructured test is executed in real-time, enforcing interface conditions using feedback controllers and actuators, and thus including the effect of interactions between the two subsystems.

Although the method was initially introduced for studying the mechanical behavior of structures exposed to extreme base motions [6] and wind/wave loads [11–13], an emerging area for the application of this testing method is to consider thermal effects on structures, and especially the extreme environmental conditions that structures may be exposed to in space. Thermal hybrid simulation has been realized by imposing thermal heat loads on experimental elements to assess their performance under thermal stresses due to fire [9,14–17]. Thermomechanical hybrid simulation has thus far aimed to assess a member's dynamic structural response to high-temperature loads, with thermal loading consisting of heating using a furnace to supply the heating load [9,14,15,17]. In these studies, the numerical substructure is not typically exposed to the heat emitted from the physical substructure. The thermal disturbances are also applied directly to the experimental substructure, thus limiting the thermal behavior to consider only one-way thermal interactions. Additionally, the interface between the experiment and numerical substructures is concentrated at one or just a few degrees of freedom (DOF), whereas systems involving thermal stresses often involve heating and cooling over a continuous region or surface.

Based on current RTHS research efforts, several gaps have been identified that have prevented researchers from tackling more complex problems [18]. A major challenge is the development and mechanical design of actuators or transfer systems to impose new interface conditions [19,20], such as distributed loads over continuous regions. New transfer system configurations can expand hybrid testing applications to multiphysics problems, such as using RTHS for the testing of complex space systems [21,22]. Additionally, one of the main reasons to perform RTHS is to capture the true behavior of the experimental subsystem, which in most cases is unknown. Thus, validating RTHS results against numerical analysis remains a challenge. As RTHS methods and applications grow in complexity, such does the need for systematic procedures for the overall evaluation and validation of RTHS tests [6,23]. Performance indicators have been developed that can be computed in advance to predict the success of a test [24]. Systematic approaches that evaluate the performance of RTHS results for the design of controllers and controlling techniques remain challenging.

This study presents a novel thermomechanical RTHS framework developed to enable researchers to perform realistic experiments considering two-way thermal coupling between a numerical and an experimental subsystem. The framework is developed and numerically demonstrated for implementation in a two-layer heat transfer system, with each layer having different thermal and material properties. The system is partitioned by breaking the two layers into an outer numerical layer and an inner physical layer. The thermal load is applied to the outer layer, while the focus of the experiment is the response of the inner physical layer. At the interface, a transfer system is employed to enforce the distributed thermal boundary conditions along the

Received 30 January 2023; revision received 0 ; accepted for publication 19 February 2023; published online 11 April 2023. Copyright © 2023 by the authors. Published by the American Institute of Aeronautics and Astronautics, Inc., with permission. All requests for copying and permission to reprint should be submitted to CCC at www.copyright.com; employ the eISSN 1533-385X to initiate your request. See also AIAA Rights and Permissions www.aiaa.org/randp.

*Graduate Research Assistant, Lyles School of Civil Engineering; montoyah@purdue.edu (Corresponding Author).
†Professor, Lyles School of Civil Engineering and School of Mechanical Engineering.
‡Research Scientist, School of Mechanical Engineering; also Assistant Professor, Facultad de Ingeniería Mecánica y Ciencias de la Producción, Escuela Superior Politécnica del Litoral, Guayaquil, Ecuador.
§Senior Research Engineer—Control Systems.
¶Graduate Research Assistant, School of Mechanical Engineering.
**Assistant Professor of Mechanical Engineering, School of Mechanical Engineering.

Downloaded by NASA LANGLEY RESEARCH CENTER on November 13, 2023 | http://arc.aiaa.org | DOI: 10.2514/1.J062857

experimental subsystem surface, and measurements of the physical system capture the thermal coupling to be fed back to the numerical subsystem. A new thermal transfer system, along with the design of a *thermal actuator*, is introduced to impose thermal interface conditions leveraging RTHS capabilities. Potential applications for this thermomechanical RTHS framework include deep space structures and arctic or deep ocean systems. The thermomechanical RTHS is illustrated through an example considering the influence of temperature on a lunar habitat. Additionally, we establish a systematic approach to developing control and performance assessment measures for such RTHS experiments. Finally, acceptance criteria specific to thermomechanical RTHS are established. The results demonstrate that thermomechanical RTHS is feasible to enable realistic testing and that careful attention must be paid to the design of the controller to ensure that researchers can meet their testing objectives.

The technical approach is discussed in Sec. II. The heat conduction problem is formulated, and the thermal actuator components are introduced in Sec. III. The system dynamics for the control plant are described in Sec. IV, and the control and performance metrics are established in Sec. V. An illustrative example is described in Sec. VI. Finally, we share the conclusions in Sec. VII.

## II. Technical Approach

The framework for the thermomechanical RTHS testing in this study, strictly from the heat conduction standpoint, is defined using a block diagram in Fig. 1. Here it is assumed that the studied structural system is divided into two layers, and the outer layer is subjected to a disturbance that takes the form of a temperature fluctuation, which has a heat flux effect on the structure. The testing is intended to be conducted so that the inner layer, which is the experimental substructure, will experience sufficiently similar thermal effects. Thus, the transfer system provides the necessary computation, interactions, and control to achieve that objective. Here we establish the methodology to meet this goal and demonstrate using a computational example. There are three major components to this framework:

1) A numerical subsystem (left side) contains a portion of a two-layered structural system subjected to thermal loading and undergoing heat conduction, typically modeled with finite elements. This subsystem takes in an external input, generating the desired interface response imposed on the experimental subsystem.

2) An experimental subsystem (right side) is realized physically in a laboratory setup and contains the remaining portion of the two-layered structural system.

3) A thermal transfer system (inside the dashed box) enforces the interaction conditions between the numerical and experimental subsystems at the boundary where they meet.

The input to the test is the external temperature on the structure's outer (numerical) layer, which is input into the numerical model, as shown in Fig. 1. The numerical model is used to compute the resulting inputs to the experimental subsystem, known as the desired response, and also takes in the response from the experimental subsystem.

The thermal transfer system consists of the physical equipment needed to realize the desired response in the experimental subsystem. It may take various forms, and one realization is discussed in the illustrative example in this paper. Actuators have dynamics, and a controller is needed to compensate for any time lags due to the presence of the thermal actuator. Thus, the controller block generates the command signal for the control plant (i.e., the thermal actuator plus the experimental subsystem). The measured response from the experimental subsystem is fed back to the thermal transfer system. This feedback signal plays two roles. In the control feedback loop, it is used by the observer block to estimate the experimental subsystem states from the measured temperature response. In the RTHS feedback loop, the state estimation block calculates the unmeasured experimental states from available measurements for the next numerical integration step. It is important to note that, even though these two estimation blocks may perform similar operations, their purpose is different, as discussed further in subsequent sections of this paper.

To realize the interface conditions, a controller is needed to compensate for the transfer system dynamics and potential interactions with the physical substructure. Regardless of the control algorithm used, the control requirements must be established to meet the needs of a given experiment. Thus, in addition to the thermomechanical RTHS problem formulation, a systematic approach is developed to determine those transfer system control requirements to conduct RTHS generally with high confidence.

Unlike traditional control approaches, we developed a systematic approach to establish control criteria, shown in Fig. 2. The main components of the approach include developing a controller set, control metrics, and performance metrics. Our approach is developed to expand the evaluation and implementation of RTHS experiments to more challenging problems, such as transfer systems with multiple components, interconnected two-dimensional (2D) and three-dimensional (3D) systems, or thermal experiments performed inside a laboratory with controlled temperature conditions.

The controller set and control metrics are related to tracking the desired input to the experimental subsystem, i.e., a local evaluation. In contrast, the performance metrics evaluate the global performance of the RTHS approach through a comparison to a reference problem. Because the reference system test typically cannot be performed due to its scale or cost, a model must be assumed. Four phases are defined to establish the control requirements: control metrics development and verification, performance metrics development and verification, control requirements generation, and controller design.

The control metrics development and verification phase is performed by simulating a set of candidate controllers when applied to the control plant (i.e., the transfer system and experimental subsystem). Candidate controllers may be designed using various control strategies and methods. Based on the dynamics of the control plant, control metrics are adopted to quantitatively evaluate the controller's behavior. Recall that these control metrics are exclusively related to the ability to effectively enforce the desired temperature on the control plant, i.e., tracking. In this phase, the goal is to assess how well each candidate controller achieves proper tracking with minimum error and verify that the control approach is properly achieving

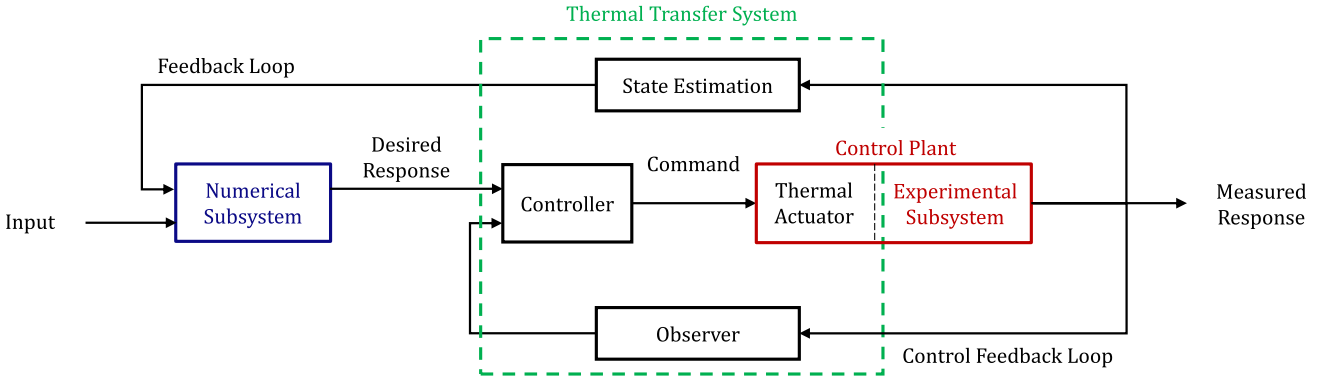



**Fig. 1 Control block diagram of thermomechanical RTHS framework.**

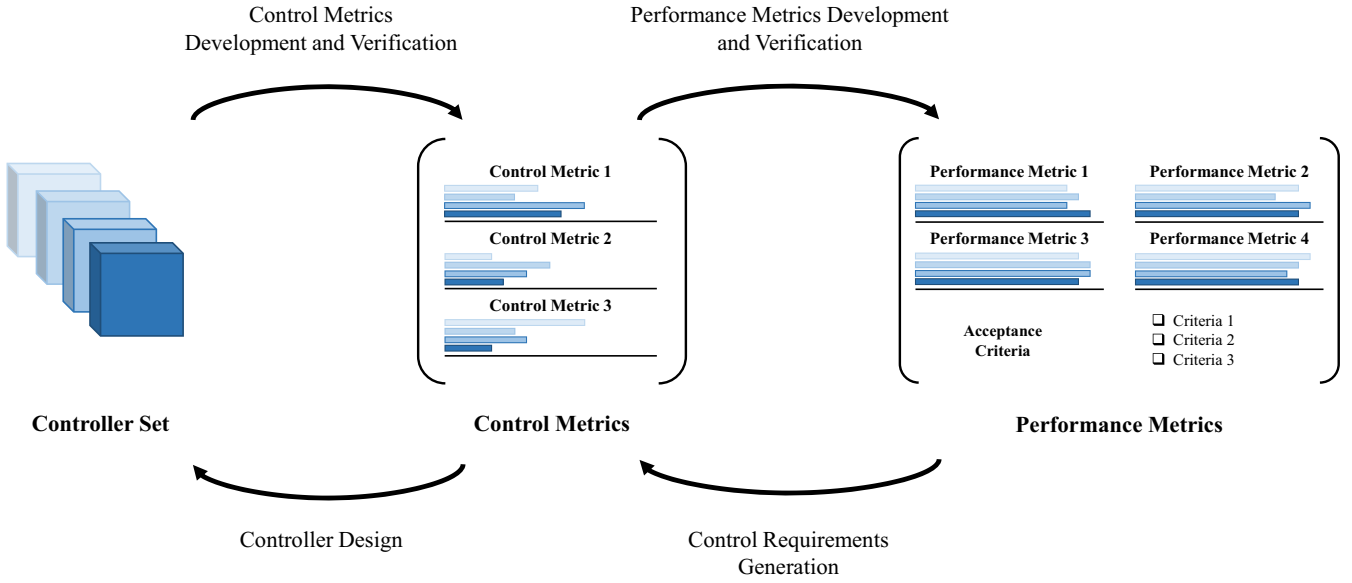



**Fig. 2 Diagram of the systematic approach for developing control criteria for RTHS.**

its goal. Threshold values are then established for the control metrics. Controllers that satisfy this threshold move on to the next phase.

Simulations of the entire RTHS system are then executed to assess the global RTHS performance. Global performance must be assessed with a reference system, typically a model of the ideal thermomechanical system with the same external input. The goal is to quantify how well the controller reduces the global error at the numerical and experimental subsystems interface and verify that the adopted control approach fulfilling its goal with minimum error. Threshold values are then established for the performance metrics. Once this step is done, a mapping is available between local and global performance to identify the control strategies that have the most favorable performance. The control strategies that best meet the global performance metrics are used to generate control requirements.

The performance metrics can also be used to define the acceptance criteria by which one would determine if an RTHS transfer system controller or control strategy is acceptable for its intended use. Acceptance criteria are part of a whole control strategy defined to perform RTHS testing with high confidence and consistency and yield accurate results that reflect reality as much as possible. In addition, acceptance criteria are needed for different types of RTHS to be considered standard testing procedures, such as shake table testing for earthquake engineering. Currently, acceptance criteria do not exist for any RTHS application.

Once the control metrics are mapped to the performance metrics, we turn to the return path. Here the control requirements generation phase involves identifying strategies that reduce tracking and global errors. The set strategies determine the confidence or error thresholds for testing objectives and serve as the standards for redesigning or assessing controller sets available to perform RTHS, as shown in the final phase.

The next section discusses the thermomechanical RTHS framework specifically for a heat conduction problem.

## III. Problem Formulation: Thermomechanical RTHS

Consider a system that consists of two layers of materials subjected to time-varying thermal loading, as shown in Fig. 3. The top layer is exposed to an external thermal load, and the bottom layer responds

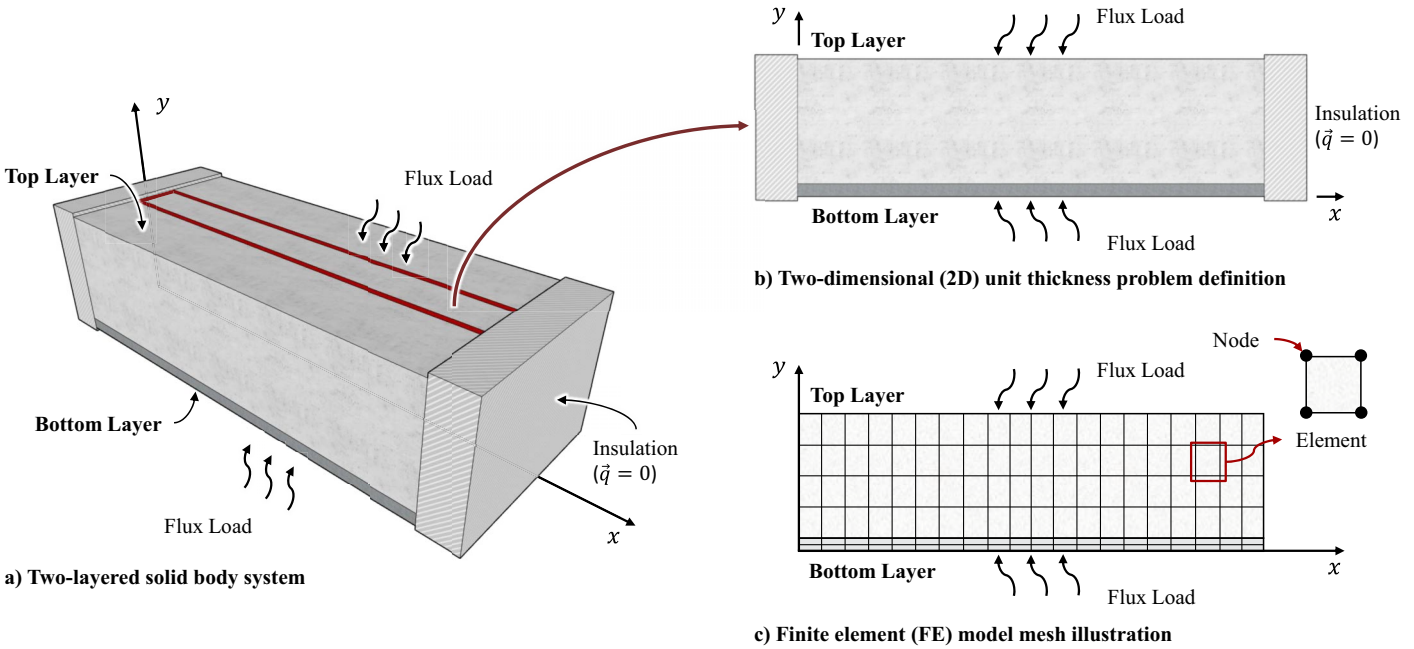



**Fig. 3 The problem formulation illustration for a 2D, two-layered finite-element solid body.**

Downloaded by NASA LANGLEY RESEARCH CENTER on November 13, 2023 | http://arc.aiaa.org | DOI: 10.2514/1.J062857

Downloaded by NASA LANGLEY RESEARCH CENTER on November 13, 2023 | http://arc.aiaa.org | DOI: 10.2514/1.J062857

according to the governing physics and internal thermal load. To formulate the RTHS problem, we first consider a model of the reference system, which is the entire system shown, and then partition the system into numerical and experimental subsystems. The partitioned system, under ideal conditions, would behave similarly to the reference system. However, the equipment needed to enforce boundary conditions in the laboratory has dynamics and limitations, and thus it would be ideal.

### A. Reference System

A finite element model of a two-layered structural system subjected to thermal loading is developed to replicate the physics of transient heat transfer through solid bodies. For illustration, the analysis of a two-layered system shown in Fig. 3a is reduced to a 2D analysis by considering a slice with a unit-thickness that is perpendicular to the $x$–$y$ plane, as shown in Figs. 3b and 3c. This model serves as the reference system. The system has a length $L$ and height $H$. Several assumptions are made to develop the finite element model. First, the physics represented by the model herein allows the dynamics for thermal conduction only. Other thermal processes, such as convection and radiation, are not considered, enabling a simplified thermomechanical system to illustrate RTHS. The material properties are assumed to be homogeneous and isotropic for all elements, with linear thermal behavior.

The finite element problem formulation for this transient heat conduction analysis is derived from the following governing differential equation [25]:

$$\rho C_p \frac{\partial T}{\partial t} = \frac{\partial}{\partial x}\left(k\frac{\partial T}{\partial x}\right) + \frac{\partial}{\partial y}\left(k\frac{\partial T}{\partial y}\right) + q_v \tag{1}$$

where the relevant thermal-material properties are density $\rho$, specific heat capacity $C_p$, and isotropic thermal conductivity $k$, with volumetric internal heat generation $q_v$ in the solid body. This equation governs the temperature distribution across the solid body as a function of space and time, $T(x, y, t)$, by defining initial and boundary conditions (predefined temperatures and heat fluxes). Heat fluxes can be position dependent, time dependent, or surface temperature dependent. For example, in Fig. 3, the system is assumed to be insulated at both vertical ends ($x = 0$ and $x = L$), restricting the heat flux to $\vec{q} = 0$.

Applying the finite element method, the nodal temperature through an element is specified by its shape function given by

$$T^{\mathrm{el}}(x, y, t) = \sum_{j=1}^{n_{\mathrm{en}}} T_j^{\mathrm{el}} \cdot \Phi_j^{\mathrm{el}}(x, y, t) = [\Phi^{\mathrm{el}}]\boldsymbol{T}^{\mathrm{el}} \tag{2}$$

where $\Phi^{\mathrm{el}}$ is the element shape function matrix, $\boldsymbol{T}^{\mathrm{el}}$ is the element temperature vector, and $n_{\mathrm{en}}$ represents the number of nodes of the element. After applying the Galerkin method and Green's theorem [25] to Eq. (1), a summation over the element domain is obtained. Finally, the 2D transient heat conduction analysis is given by

$$[\mathrm{M}^{\mathrm{el}}]\dot{\boldsymbol{T}}^{\mathrm{el}} + [\mathrm{K}^{\mathrm{el}}]\boldsymbol{T}^{\mathrm{el}} = \boldsymbol{F}^{\mathrm{el}} \tag{3}$$

where $\mathrm{M}^{\mathrm{el}}$ is the capacitance matrix, $\mathrm{K}^{\mathrm{el}}$ is the conductance matrix, $\boldsymbol{F}^{\mathrm{el}}$ is the flux load vector, and $\dot{\boldsymbol{T}}^{\mathrm{el}}$ is the temperature gradient vector. The element load vector $\boldsymbol{F}^{\mathrm{el}}$ accounts for the convective flux load at the outer boundary elements. The element conductance, $[\mathrm{K}^{\mathrm{el}}]$, and capacitance, $[\mathrm{M}^{\mathrm{el}}]$, matrices are assembled by

$$[\mathrm{K}^{\mathrm{el}}] = \int_{\Omega^{\mathrm{el}}} [\mathrm{B}^{\mathrm{el}}]^{\mathrm{T}}[\mathrm{D}^{\mathrm{el}}][\mathrm{B}^{\mathrm{el}}]\,\mathrm{d}\Omega \tag{4}$$

$$[\mathrm{M}^{\mathrm{el}}] = \int_{\Omega^{\mathrm{el}}} \rho C_p [\Phi^{\mathrm{el}}]^{\mathrm{T}}[\Phi^{\mathrm{el}}]\,\mathrm{d}\Omega \tag{5}$$

where $[\mathrm{B}^{\mathrm{el}}]$ and $[\mathrm{D}^{\mathrm{el}}]$ are the temperature gradient matrix and conductivity matrix, respectively, across the element domain $\Omega^{\mathrm{el}}$. The conductivity matrix $[\mathrm{D}^{\mathrm{el}}]$ for a four-node rectangular element, as shown in Fig. 3c, has the form

$$[\mathrm{D}^{\mathrm{el}}] = \begin{bmatrix} k_{xx} & k_{xy} \\ k_{yx} & k_{yy} \end{bmatrix} \tag{6}$$

Because the conductivity for this problem formulation is isotropic, $k_{xx} = k_{yy}$ and $k_{xy} = k_{yx} = 0$.

The system shown in Fig. 3 has two layers, each with its own thermal properties. Figure 3c illustrates the mesh used for the finite element model containing elements representing each material layer. The global matrices for the two-layered system are assembled, yielding the global matrices for the two-layered 2D transient heat conduction model, referred to as the reference model, which is presented as

$$[\mathrm{M_r}]\dot{\boldsymbol{T}}_{\mathrm{r}} + [\mathrm{K_r}]\boldsymbol{T}_{\mathrm{r}} = \boldsymbol{F}_{\mathrm{r}} \tag{7}$$

where $[\mathrm{M_r}]$ is the global capacitance matrix, $[\mathrm{K_r}]$ is the global conductance matrix, $\boldsymbol{F}_{\mathrm{r}}$ is the global flux load vector, and $\boldsymbol{T}_{\mathrm{r}}$ and $\dot{\boldsymbol{T}}_{\mathrm{r}}$ are the global temperature and temperature gradient vectors, respectively. The $(\cdot)_{\mathrm{r}}$ subscript denotes reference.

### B. System Partitioning

The partitioning of the transient heat conduction system is shown in Fig. 4. The numerical subsystem contains the top layer, while the bottom layer represents the experimental subsystem. Both subsystems interact at the nodes through the interface temperature, and heat flux exchanged between the two layers. Henceforth, the flux load in the boundary elements will be denoted as the numerical and experimental flux load for each subsystem, respectively.

To implement RTHS, the reference model is partitioned into numerical and experimental subsystems. The thermal reference model is a continuous-surface, solid-body system. Thus, both subsystems share boundaries through interface element nodes. The reference matrices are thus partitioned as follows:

$$[\mathrm{M_r}] = \begin{bmatrix} \mathrm{M_e} & \mathrm{M_{e,i}} & 0 \\ \mathrm{M_{i,e}} & \mathrm{M_i} & \mathrm{M_{i,n}} \\ 0 & \mathrm{M_{n,i}} & \mathrm{M_n} \end{bmatrix}, \quad [\mathrm{K}_r] = \begin{bmatrix} \mathrm{K_e} & \mathrm{K_{e,i}} & 0 \\ \mathrm{K_{i,e}} & \mathrm{K_i} & \mathrm{K_{i,n}} \\ 0 & \mathrm{K_{n,i}} & \mathrm{K_n} \end{bmatrix} \tag{8}$$

The $(\cdot)_{\mathrm{e}}$, $(\cdot)_{\mathrm{i}}$, and $(\cdot)_{\mathrm{n}}$ subscripts denote experimental, interface, and numerical, respectively. The off-diagonal matrix entries represent the coupling between the experimental and numerical nodes with the interface nodes. Likewise, the temperature, temperature gradient, and flux load vectors can be partitioned into the experimental, interface, and numerical nodes:

$$\boldsymbol{T}_{\mathrm{r}} = \begin{Bmatrix} \boldsymbol{T}_{\mathrm{e}} \\ \boldsymbol{T}_{\mathrm{i}} \\ \boldsymbol{T}_{\mathrm{n}} \end{Bmatrix}, \quad \dot{\boldsymbol{T}}_{\mathrm{r}} = \begin{Bmatrix} \dot{\boldsymbol{T}}_{\mathrm{e}} \\ \dot{\boldsymbol{T}}_{\mathrm{i}} \\ \dot{\boldsymbol{T}}_{\mathrm{n}} \end{Bmatrix}, \quad \boldsymbol{F}_{\mathrm{r}} = \begin{Bmatrix} \boldsymbol{F}_{\mathrm{e}} \\ \boldsymbol{F}_{\mathrm{i}} \\ \boldsymbol{F}_{\mathrm{n}} \end{Bmatrix} \tag{9}$$

Substituting Eqs. (8) and (9) into Eq. (7), the transient heat conduction problem can be rewritten as

$$\begin{bmatrix} \mathrm{M_e} & \mathrm{M_{e,i}} & 0 \\ \mathrm{M_{i,e}} & \mathrm{M_i} & \mathrm{M_{i,n}} \\ 0 & \mathrm{M_{n,i}} & \mathrm{M_n} \end{bmatrix} \begin{Bmatrix} \dot{\boldsymbol{T}}_{\mathrm{e}} \\ \dot{\boldsymbol{T}}_{\mathrm{i}} \\ \dot{\boldsymbol{T}}_{\mathrm{n}} \end{Bmatrix} + \begin{bmatrix} \mathrm{K_e} & \mathrm{K_{e,i}} & 0 \\ \mathrm{K_{i,e}} & \mathrm{K_i} & \mathrm{K_{i,n}} \\ 0 & \mathrm{K_{n,i}} & \mathrm{K_n} \end{bmatrix} \begin{Bmatrix} \boldsymbol{T}_{\mathrm{e}} \\ \boldsymbol{T}_{\mathrm{i}} \\ \boldsymbol{T}_{\mathrm{n}} \end{Bmatrix} = \begin{Bmatrix} \boldsymbol{F}_{\mathrm{e}} \\ \boldsymbol{F}_{\mathrm{i}} \\ \boldsymbol{F}_{\mathrm{n}} \end{Bmatrix} \tag{10}$$

The interface nodes of the continuous surface contain material properties of both the numerical and the experimental subsystems. Thus, the capacitance and conductance interface matrices are influenced by the properties of both layers

$$[\mathrm{M_i}] = [\mathrm{M_i^{(p)}}] + [\mathrm{M_i^{(c)}}], \quad [\mathrm{K_i}] = [\mathrm{K_i^{(p)}}] + [\mathrm{K_i^{(c)}}] \tag{11}$$

The $(\cdot)^{(\mathrm{p})}$ and $(\cdot)^{(\mathrm{c})}$ superscripts denote the physical and cyber (numerical) node properties of the interface nodes.

Using Eq. (11) and the problem formulation in Eq. (10), we can separate the thermal model into two models representing the numerical and experimental subsystems. The interactions between the two subsystems are captured through their respective inputs and outputs.

The numerical subsystem can be written as follows:

$$\begin{bmatrix} \mathrm{M_i^{(c)}} & \mathrm{M_{i,n}} \\ \mathrm{M_{n,i}} & \mathrm{M_n} \end{bmatrix} \begin{Bmatrix} \dot{\boldsymbol{T}}_\mathrm{i} \\ \dot{\boldsymbol{T}}_\mathrm{n} \end{Bmatrix} + \begin{bmatrix} \mathrm{K_i^{(c)}} & \mathrm{K_{i,n}} \\ \mathrm{K_{n,i}} & \mathrm{K_n} \end{bmatrix} \begin{Bmatrix} \boldsymbol{T}_\mathrm{i} \\ \boldsymbol{T}_\mathrm{n} \end{Bmatrix} = \begin{Bmatrix} \boldsymbol{F}_\mathrm{i} \\ \boldsymbol{F}_\mathrm{n} \end{Bmatrix} - \begin{bmatrix} \mathrm{M_{i,e}} & \mathrm{M_i^{(p)}} \\ 0 & 0 \end{bmatrix} \begin{Bmatrix} \dot{\boldsymbol{T}}_\mathrm{e} \\ \dot{\boldsymbol{T}}_\mathrm{i} \end{Bmatrix} - \begin{bmatrix} \mathrm{K_{i,e}} & \mathrm{K_i^{(p)}} \\ 0 & 0 \end{bmatrix} \begin{Bmatrix} \boldsymbol{T}_\mathrm{e} \\ \boldsymbol{T}_\mathrm{i} \end{Bmatrix} \tag{12}$$

Hereafter, the numerical capacitance and conductance matrices from the left-hand side of Eq. (12) will be referred as

$$[\mathrm{M_N}] = \begin{bmatrix} \mathrm{M_i^{(c)}} & \mathrm{M_{i,n}} \\ \mathrm{M_{n,i}} & \mathrm{M_n} \end{bmatrix}, \quad [\mathrm{K_N}] = \begin{bmatrix} \mathrm{K_i^{(c)}} & \mathrm{K_{i,n}} \\ \mathrm{K_{n,i}} & \mathrm{K_n} \end{bmatrix} \tag{13}$$

The two last terms from the right-hand side of the first row of Eq. (12) can be denoted as

$$\boldsymbol{f}_\mathrm{i}^{(\mathrm{p})} = \begin{bmatrix} \mathrm{M_{i,e}} & \mathrm{M_i^{(p)}} \end{bmatrix} \begin{Bmatrix} \dot{\boldsymbol{T}}_\mathrm{e} \\ \dot{\boldsymbol{T}}_\mathrm{i} \end{Bmatrix} + \begin{bmatrix} \mathrm{K_{i,e}} & \mathrm{K_i^{(p)}} \end{bmatrix} \begin{Bmatrix} \boldsymbol{T}_\mathrm{e} \\ \boldsymbol{T}_\mathrm{i} \end{Bmatrix} \tag{14}$$

where $\boldsymbol{f}_\mathrm{i}^{(\mathrm{p})}$ is the feedback heat flux at the interface associated with the experimental response.

The experimental subsystem is represented by

$$[\mathrm{M_e}]\dot{\boldsymbol{T}}_\mathrm{e} + [\mathrm{K_e}]\boldsymbol{T}_\mathrm{e} = \boldsymbol{F}_\mathrm{e} - [\mathrm{M_{e,i}}]\dot{\boldsymbol{T}}_\mathrm{i} - [\mathrm{K_{e,i}}]\boldsymbol{T}_\mathrm{i} \tag{15}$$

Equations (12) and (15) can be written in state-space form. The state-space representation of the numerical subsystem, indicated by the subscript $(\cdot)_\mathrm{N}$, is given by

$$\begin{bmatrix} \dot{z}_\mathrm{N} \\ \boldsymbol{y}_\mathrm{N} \end{bmatrix} = \begin{bmatrix} \mathrm{A_N} & \mathrm{B_N} \\ \mathrm{C_N} & \mathrm{D_N} \end{bmatrix} \begin{bmatrix} z_\mathrm{N} \\ \boldsymbol{u}_\mathrm{N} \end{bmatrix} \tag{16}$$

where $[\mathrm{A_N}]$ is the state matrix, $[\mathrm{B_N}]$ the input matrix, $[\mathrm{C_N}]$ the output matrix, $[\mathrm{D_N}]$ the feedthrough matrix, $z_\mathrm{N}$ the state vector given by $[\boldsymbol{T}_\mathrm{i} \quad \boldsymbol{T}_\mathrm{n}]^\mathrm{T}$, $\boldsymbol{u}_\mathrm{N}$ the input vector given by $[\boldsymbol{F}_\mathrm{i} \quad \boldsymbol{F}_\mathrm{n} \quad \boldsymbol{f}_\mathrm{i}^{(p)} \quad \boldsymbol{0}]^\mathrm{T}$, and $\boldsymbol{y}_\mathrm{N}$ the output vector given by $[\boldsymbol{T}_\mathrm{i} \quad \boldsymbol{T}_\mathrm{n} \quad \dot{\boldsymbol{T}}_\mathrm{i} \quad \dot{\boldsymbol{T}}_\mathrm{n}]^\mathrm{T}$. The numerical subsystem state-space matrices in Eq. (16) are defined as

$$[\mathrm{A_N}] = \begin{bmatrix} -\mathrm{M_N^{-1}K_N} \end{bmatrix}; \quad [\mathrm{B_N}] = \begin{bmatrix} \mathrm{M_N^{-1}} & -\mathrm{M_N^{-1}} \end{bmatrix};$$
$$[\mathrm{C_N}] = \begin{bmatrix} \mathrm{I} \\ -\mathrm{M_N^{-1}K_N} \end{bmatrix}; \quad [\mathrm{D_N}] = \begin{bmatrix} 0 & 0 \\ \mathrm{M_N^{-1}} & -\mathrm{M_N^{-1}} \end{bmatrix} \tag{17}$$

The state-space form of the experimental subsystem, indicated by the subscript $(\cdot)_\mathrm{E}$, is given by

$$\begin{bmatrix} \dot{z}_\mathrm{E} \\ \boldsymbol{y}_\mathrm{E} \end{bmatrix} = \begin{bmatrix} \mathrm{A_E} & \mathrm{B_E} \\ \mathrm{C_E} & \mathrm{D_E} \end{bmatrix} \begin{bmatrix} z_\mathrm{E} \\ \boldsymbol{u}_\mathrm{E} \end{bmatrix} \tag{18}$$

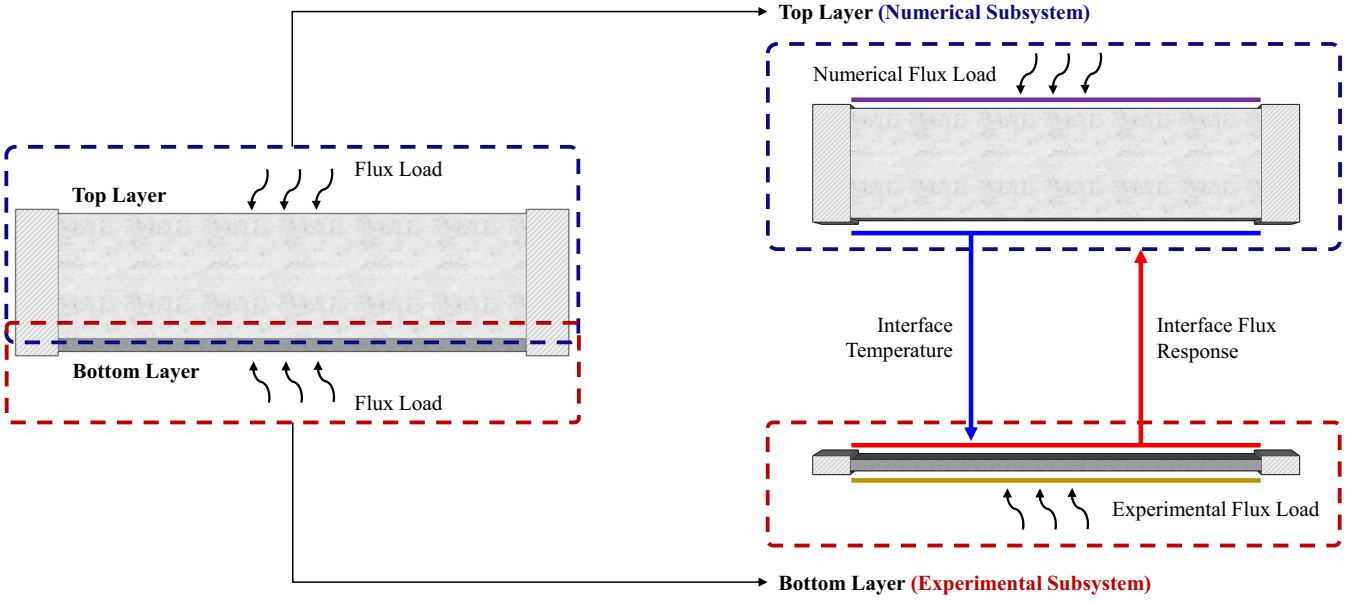
where $[\mathrm{A_E}]$ is the state matrix, $[\mathrm{B_E}]$ the input matrix, $[\mathrm{C_E}]$ the output matrix, $[\mathrm{D_E}]$ the feedthrough matrix, $z_\mathrm{E}$ the state vector given by $[\boldsymbol{T}_\mathrm{E}]^\mathrm{T}$, $\boldsymbol{u}_\mathrm{E}$ the input vector given by $[\boldsymbol{F}_\mathrm{E} \quad \dot{\boldsymbol{T}}_\mathrm{i} \quad \boldsymbol{T}_\mathrm{i}]^\mathrm{T}$, and $\boldsymbol{y}_\mathrm{E}$ the output vector given by $[\boldsymbol{T}_\mathrm{E} \quad \dot{\boldsymbol{T}}_\mathrm{E}]^\mathrm{T}$. The experimental subsystem state-space matrices in Eq. (18) are defined as

$$[\mathrm{A_E}] = \begin{bmatrix} -\mathrm{M_e^{-1}K_e} \end{bmatrix}; \quad [\mathrm{B_E}] = \begin{bmatrix} \mathrm{M_e^{-1}} & -\mathrm{M_e^{-1}M_{e,i}} & -\mathrm{M_e^{-1}K_{e,i}} \end{bmatrix};$$
$$[\mathrm{C_E}] = \begin{bmatrix} \mathrm{I} \\ -\mathrm{M_e^{-1}K_e} \end{bmatrix}; \quad [\mathrm{D_E}] = \begin{bmatrix} 0 & 0 & 0 \\ -\mathrm{M_e^{-1}} & -\mathrm{M_e^{-1}M_{e,i}} & -\mathrm{M_e^{-1}K_{e,i}} \end{bmatrix} \tag{19}$$

From Fig. 4 and in the partitioned Eqs. (12) and (15), notice that the inputs to the numerical subsystem are the heat flux load vector plus the feedback heat flux response from the experimental subsystem. The outputs of the numerical subsystem are selected such that they are the inputs to the experimental subsystem. Likewise, the outputs of the experimental subsystem are selected such that they are inputs to the numerical subsystem.

### C. Thermal Transfer System Components

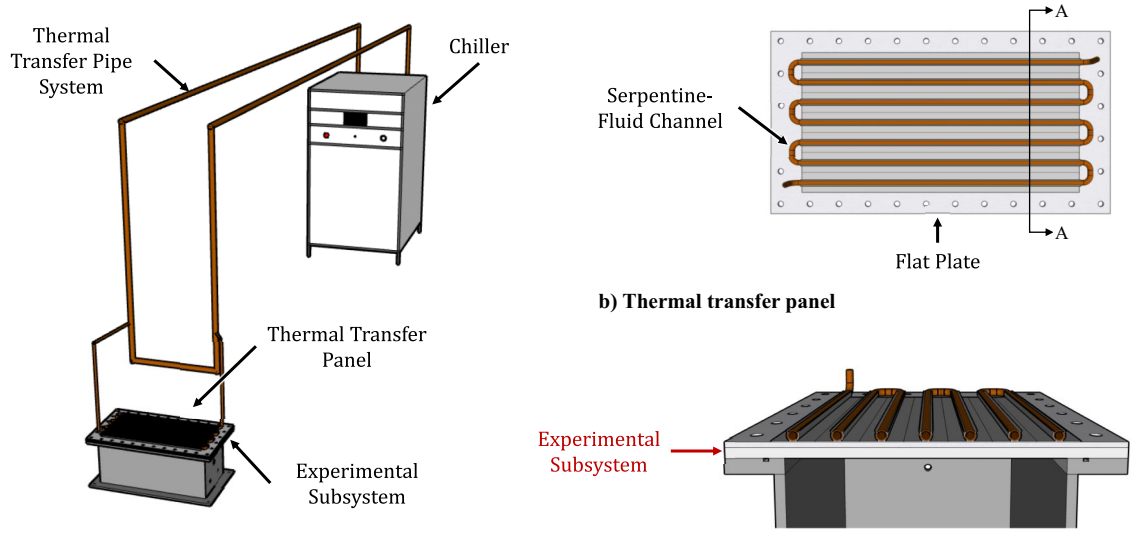
The thermal actuator is used to impart the desired temperature at the interface between the numerical and the experimental subsystems.




a) System partitioning schematic b) Partitioned RTHS system

**Fig. 4 Two-dimensional, two-layer system RTHS partitioning schematic.**

Downloaded by NASA LANGLEY RESEARCH CENTER on November 13, 2023 | http://arc.aiaa.org | DOI: 10.2514/1.J062857




**a) Thermomechanical RTHS control plant (thermal actuator system and experimental subsystem)**

**b) Thermal transfer panel**

**c) Cross-section A-A**

**Fig. 5 Thermomechanical RTHS control plant: *thermal actuator* components with the experimental subsystem.**

There is actually a coupling between these two subsystems enforced with a feedback loop involving temperature and heat flux. The thermal actuator has a similar design to the panel surface temperature control system in [26]. The three main components are a cryogenic chiller that transfers heat to the fluid, a piping system to circulate the fluid to the experimental subsystem, and a thermal transfer panel that acts at the interface with the experimental subsystem. A schematic diagram showing how these components are set up is shown in Fig. 5.

A *chiller* transfers heat to and from a system by adjusting its temperature through a heat transfer cycle and circulating fluid. A chiller, in general, is intended for cooling. However, the chiller presented in this framework also has heating capabilities. Therefore, a cryogenic chiller with dual heat exchange capacity is chosen to enable a wide range of desired temperatures for the experimental subsystem.

The pipe system and panel are the thermal actuator components used to circulate the fluid that transfers heat to the experimental subsystem. The chiller supplies fluid to the thermal transfer pipe system, shown in Fig. 5, which is responsible for circulating the heat transfer fluid (HTF) from the chiller to the *thermal transfer panel*. A common approach for building the transfer panel is the "serpentine-channel cooling plate" design, involving a flat plate with fluid channels, often used in liquid cooling systems [26–28]. The serpentine-channel layout of the pipes on top of the panel (see Fig. 5b) increases the contact area with the panel [27]. The circulating fluid is the medium by which heat transfers to or from the thermal transfer flat plate and then to the experimental subsystem. In addition, heat spreaders are often used between pipe channels to facilitate the heat transfer between the piping arrangement and the flat plate. The thermal transfer panel is thus in direct contact with the upper surface of the experimental subsystem, as shown in Fig. 5c. The thermal transfer panel, through conduction, serves as a heat exchanger between the HTF and the experimental subsystem. The challenge in thermomechanical RTHS is to enforce the desired temperature at the interface between the numerical and experimental subsystems, given that the tests are performed in a temperature-controlled laboratory with heat losses to the surroundings.

### D. RTHS Implementation and Limitations

The block diagram for the complete RTHS implementation is shown in Fig. 6. The external flux load vector for the numerical subsystem, $\boldsymbol{F}_u = [\,\boldsymbol{F}_i \quad \boldsymbol{F}_n\,]^T$, and feedback flux vector $\boldsymbol{F}_f$ are inputs to the numerical subsystem. The numerical subsystem determines and outputs the desired interface temperature vector $\boldsymbol{T}_{i,d}$ using the state-space model. This vector $\boldsymbol{T}_{i,d}$ is then input to the controller as the desired temperature vector. A feedback controller must be designed

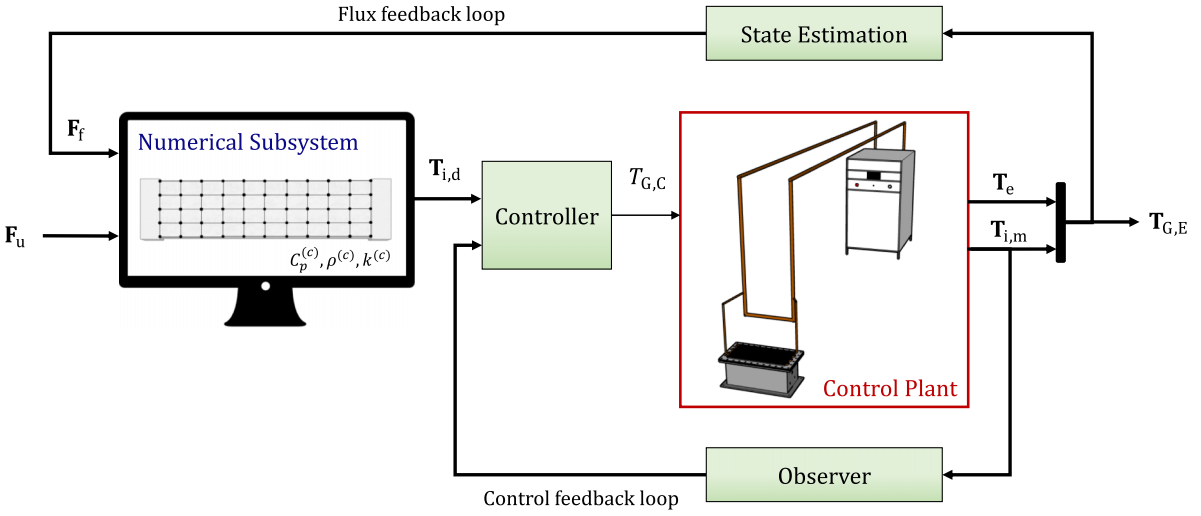



**Fig. 6 Schematic block diagram of the thermomechanical RTHS problem.**

Downloaded by NASA LANGLEY RESEARCH CENTER on November 13, 2023 | http://arc.aiaa.org | DOI: 10.2514/1.J062857

Downloaded by NASA LANGLEY RESEARCH CENTER on November 13, 2023 | http://arc.aiaa.org | DOI: 10.2514/1.J062857

to generate an appropriate command temperature signal $T_{G,C}$, to achieve the desired temperature when input to the thermal actuator. Feedback is provided to the controller using the measured interface temperature vector $\boldsymbol{T}_{i,m}$, which includes several temperature measurements from the experimental subsystem. The experimental temperature output vector $\boldsymbol{T}_{G,E} = [\boldsymbol{T}_e \quad \boldsymbol{T}_{i,m}]^T$ is used in the state estimation block for computing the feedback flux to be input the numerical subsystem $\boldsymbol{F}_f = [\boldsymbol{f}_i^{(p)} \quad \boldsymbol{0}]^T$.

Some assumptions and limitations are used in formulating this RTHS problem and performing the computational studies discussed here. Additionally, one should also be mindful of certain realistic experimental challenges.

1) The block diagram in Fig. 6 shows that many of the inputs and outputs, in particular to the transfer panel and the numerical subsystem, are vectors. However, the HTF entering any given thermal actuator component can only be controlled by the scalar temperature $T_{G,C}$.

2) Modeling of the dynamics of the thermal actuator components assumes spatially distributed behavior and is based on basic thermal principles limited to the available measured signals. The measured states assumed to be available for this study are temperature and flow rate.

3) The HTF properties are assumed to be constant and homogeneous for both heat-exchange cycles (cooling and heating). This study assumes that the fluid is incompressible with a stronger dependence on temperature than pressure. Thus, the pressure drops in the HTF loop through the thermal transfer pipe system are negligible.

4) The thermal panel performance has been experimentally assessed for prototype testing. Thermal transfer panel performance limits for cooling and heating modes were determined by evaluating the maximum temperature change achieved within 1 minute with the given chiller and design conditions. The maximum performance limits of the thermal panel are 4.2°C/min for cooling and 1.4°C/min for heating.

5) Thermal transfer panel designs show significant heat losses at the panel edges even with the use of insulation [26]. Air gaps between the panel and insulation have high thermal resistance and hinder the overall conductance. From experimental observations, the region with the lowest temperature error is localized in the center of the thermal transfer panel. Thus, panel edge heat losses are considered when evaluating the RTHS control tracking and performance.

6) The feedback to the numerical subsystem is the interface thermal flux, a physical state that is not modeled as an output of the thermal transfer system. Thermal flux may be measured directly using heat flux sensors or indirectly using temperature sensors. If the entire RTHS framework is executed virtually, as in this study, the state estimation block provides the interface feedback flux $\boldsymbol{f}_i^{(p)}$ by solving Eq. (14). On the other hand, suppose that the experimental subsystem is an actual experimental setup with a limited number of thermal sensors. In that case, the available boundary measurements of the experimental output $\boldsymbol{T}_{G,E}$ may be used with an estimation block (see Fig. 6) to obtain the appropriate flux vector to feedback to the numerical subsystem.

## IV. Thermal Actuator System Dynamics

Once the thermomechanical RTHS control problem is formulated, a model is needed for the thermal actuator for the control plant shown in Fig. 7.

The chiller is the first component of the thermal actuator, and the system is defined as the thermal response of the HTF supplied. The HTF reservoir is treated as a lumped-capacitance system, assuming uniform spatial behavior (the refrigerant fluid properties are constant and homogeneous). The inputs to the chiller are the command temperature $T_{G,C}$ and a set flow rate (assumed constant herein). The output is the outlet HTF temperature $T_C$, and its rate temperature change is expressed as

$$\dot{m}_{f,C} C_{p,f} \dot{T}_C = \dot{Q}_{C,load} - \dot{Q}_{C,loss} \tag{20}$$

where $\dot{m}_{f,C}$ is the constant mass flow rate of the fluid inside the chiller, $C_{p,f}$ is the specific heat capacity of the HTF, $\dot{Q}_{C,load}$ is the heat transfer rate from the chiller into the fluid, and $\dot{Q}_{C,loss}$ is the rate of thermal energy loss by convection to the ambient.

The heat load transfer into the fluid is computed by introducing an effectiveness

$$\dot{Q}_{C,load} = \epsilon \dot{Q}_{C,capacity} \tag{21}$$

where $\dot{Q}_{C,capacity}$ is the heat rate exchange design capacity of the chiller, and $\epsilon$ is the heat exchange effectiveness coefficient from the chiller to the HTF.

The heat loss to the ambient is defined as Newton's law of cooling that is described as

$$\dot{Q}_{C,loss} = h_f A_C (T_C - T_{amb}) \tag{22}$$

where $h_f$ is the HTF natural convection heat transfer coefficient, $A_C$ is the heat transfer surface inside the chiller, while $T_{amb}$ is the ambient temperature (suitably far from the heat transfer surface area). Considering in this numerical study that the ambient temperature is constant, it is ideally assumed that the lumped parameter $h_f A_C$, known as fluid-to-pipe thermal resistance due to convection, is equal to one.

From the definition of Eqs. (21) and (22), the HTF rate of temperature change in Eq. (20) is rewritten as

$$\dot{T}_C = -R_f T_C + R_f T_{amb} + \epsilon R_f \dot{Q}_{C,capacity} \tag{23}$$

The lumped parameter $R_f = 1/\dot{m}_{f,C} C_{p,f}$ is the HTF thermal resistance.

Additionally, the chiller operates by switching its heat exchange cycles on or off based on an internal tracking error, and its behavior is not symmetric for cooling and heating. Generally, chillers have a wide range of heat exchange capacities and mechanisms. A commercial chiller's controller(s) is unknown and proprietary. Thus, the chiller was modeled as a switched-mode linear time-invariant system with a switching rule triggered by the continuous state evolution of $T_C$.

The three modes of the chiller are OFF, heating, and cooling. The OFF mode describes the cycle at which the HTF flows through the chiller with no active heat exchange mechanism. The heating mode describes when the chiller generates heat and transfers it to the HTF,

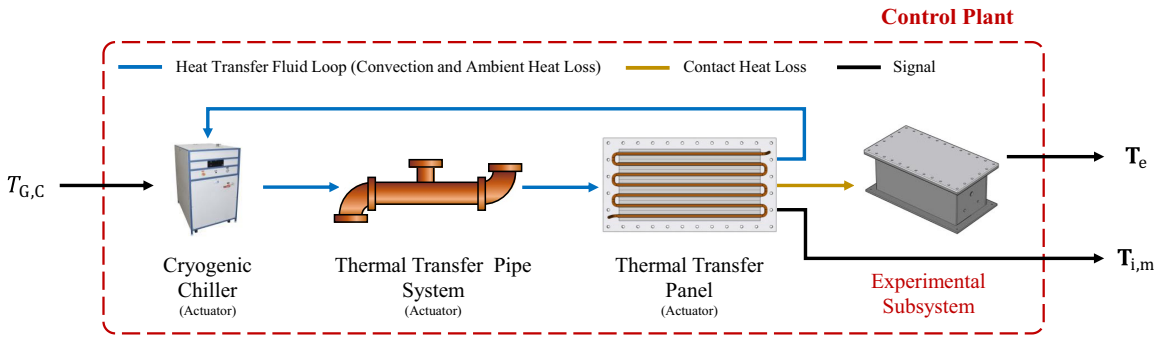



**Fig. 7 Schematic block diagram of the thermomechanical RTHS control plant.**

while the cooling mode describes the chiller cycle when heat is removed from the HTF. The state-dependent switching rule was identified as follows:

$$\sigma(T_C) = \begin{cases} 1: & -e_{\text{tol,C}} \le T_{\text{G,C}} - T_C \le e_{\text{tol,C}} \\ 2: & T_{\text{G,C}} - T_C > e_{\text{tol,C}} \\ 3: & T_{\text{G,C}} - T_C < -e_{\text{tol,C}} \end{cases} \tag{24}$$

where $\sigma$ is the switching signal or indicator, and $e_{\text{tol,C}}$ is the predetermined internal tracking error tolerance to transition modes. The temperature $T_C$ does not change because of switching modes. Thus, the switching reset condition is the state itself. The OFF, heating, and cooling modes are denoted by $\sigma = 1, 2, 3$, respectively.

The switched-controlled HTF rate of temperature change, using Eqs. (23) and (24), can be described by

$$\dot{T}_C = [A_{C,\sigma}]T_C + [B_{C,\sigma}]\boldsymbol{u}_{C,\sigma} = [A_{C,\sigma}]T_C + [B_{C,\sigma}]\begin{Bmatrix} u_C(\sigma, T_C) \\ T_{\text{amb}} \end{Bmatrix} \tag{25}$$

where $[A_{C,\sigma}]$ and $[B_{C,\sigma}]$ are the state and input matrices for switching mode $\sigma$, respectively. The input, denoted by $\boldsymbol{u}_{C,\sigma}$, is the collection of the chiller control input variable $u_C(\sigma, T_C)$ and the uncontrolled input $T_{\text{amb}}$. The control input variable $u_C$ is defined as

$$u_C(\sigma, T_C) = \begin{cases} 0 & : \quad \sigma = 1 \\ \dot{Q}_{\text{C,heat}} & : \quad \sigma = 2 \\ \dot{Q}_{\text{C,cool}} & : \quad \sigma = 3 \end{cases} \tag{26}$$

where $\dot{Q}_{\text{C,heat}}$ and $\dot{Q}_{\text{C,cool}}$ are the heating and chiller mode rate exchange design capacity, respectively. The heat rate capacity for the OFF mode is set to 0, because there is no active heat exchange taking place.

The matrices in Eq. (25) follow the form of Eq. (23) and are as follows:

$$\begin{aligned} &[A_{C,1}] = [A_{C,2}] = [A_{C,3}] = [-R_f]; \\ &[B_{C,1}] = \begin{bmatrix} 0 & R_f \end{bmatrix}; \quad [B_{C,2}] = \begin{bmatrix} \epsilon_{\text{heat}} R_f & R_f \end{bmatrix}; \quad [B_{C,3}] = \begin{bmatrix} -\epsilon_{\text{cool}} R_f & R_f \end{bmatrix} \end{aligned} \tag{27}$$

The sign convention for the load capacity of the cooling mode is to use negative when heat is being removed from the system. For all modes,

$$y_{C,\sigma} = [C_C]T_C + [D_C]\boldsymbol{u}_{C,\sigma} \tag{28}$$

where the output matrix $[C_C] = I_{1\times 1}$ and the feedthrough matrix $[D_C] = 0_{1\times 2}$.

The thermal response of the HTF in the thermal transfer pipe system is identified using a lumped capacitance approach [29]. The rate of change for the output HTF temperature of the supply pipe system $T_S$, with input $T_C$ and disturbance $T_{\text{amb}}$, is described by

$$\dot{T}_S = \frac{1}{M_{f,S} C_{p,f}} (\dot{m}_{f,S} C_{p,f} (T_C - T_S) - h_f A_S (T_S - T_{\text{amb}})) \tag{29}$$

where $M_{f,S}$ is the mass of HTF in the piping system, $\dot{m}_{f,S}$ is the piping mass flow rate, and $A_S$ is the heat transfer area in the piping system. The first term of the right-hand side of the equation is the heat transfer by convection from the chiller to the panel, i.e., the motion of the fluid itself carries heat from one place to another. The second term in the equation is the heat loss from the fluid to the pipe and the ambient, defined by Newton's law of cooling. Equation (29) can be rewritten as

$$\begin{aligned} \dot{T}_S &= -\left(\frac{\dot{m}_{f,S}}{M_{f,S}} + \frac{h_f A_S}{M_{f,S} C_{p,f}}\right) T_S + \frac{\dot{m}_{f,S}}{M_{f,S}} T_C + \frac{h_f A_S}{M_{f,S} C_{p,f}} T_{\text{amb}} \\ &= -\lambda_{S,1} T_S + \lambda_{S,2} T_C + \lambda_{S,3} T_{\text{amb}} \end{aligned} \tag{30}$$

The last component is the thermal transfer panel. As shown in Fig. 7, this component has two heat transfer mechanisms: the HTF loop and contact heat loss. The HTF loop involves the heat transfer through fluid motion in the serpentine channel and its heat loss to the ambient. The contact heat loss is the convection heat transfer between the HTF and the flat plate. The rate of change for the thermal transfer panel temperature due to the HTF loop, $T_{P,f}$, is described by

$$\begin{aligned} \dot{T}_{P,f} &= \left(\frac{\dot{m}_{f,P}}{M_{f,P}} + \frac{h_f A_{P,\text{amb}}}{M_{f,P} C_{p,f}}\right) T_{P,\mathbf{f}} + \frac{\dot{m}_{f,P}}{M_{f,P}} T_S + \frac{h_f A_{P,\text{amb}}}{M_{f,P} C_{p,f}} T_{\text{amb}} \\ &= \lambda_{P,1} T_{P,f} + \lambda_{P,2} T_S + \lambda_{P,3} T_{\text{amb}} \end{aligned} \tag{31}$$

where $M_{f,P}$ is the mass of HTF in the serpentine channel, $\dot{m}_{f,P}$ is the channel flow rate, and $A_{P,\text{amb}}$ is the heat transfer area of the panel to the environment. The rate of change for the thermal transfer panel temperature due to the contact heat loss, $T_{P,l}$, is defined as

$$\dot{T}_{P,l} = \frac{h_f A_{P,l}}{M_{P,l} C_{p,l}} T_{P,l} + \frac{h_f A_{P,l}}{M_{P,l} C_{p,l}} T_S = \lambda_{P,4} T_{P,l} + \lambda_{P,5} T_S \tag{32}$$

where $M_{P,l}$ is the mass of the thermal transfer panel plate, $C_{p,l}$ is the specific heat capacity of the plate, and $A_{P,l}$ is the heat transfer area between the fluid and the plate.

The thermal transfer panel output temperature $T_P$ can be determined by

$$T_P = w_{P,f} T_{P,f} + w_{P,l} T_{P,l} \tag{33}$$

The parameters $w_{P,f}$ and $w_{P,l}$ are the weighting factors for each heat transfer process.

The values for the lumped parameters $\lambda_{S,1}, \lambda_{S,2}, \lambda_{S,3}, \lambda_{P,1}, \lambda_{P,2}, \lambda_{P,3}, \lambda_{P,4}, \lambda_{P,5}, w_{P,f}$, and $w_{P,l}$ are determined from experimental observations.

As the HTF moves through the thermal transfer panel, the heat loss transfer areas from input temperature $T_S$ increase. Thus, the temperature through the thermal transfer panel changes from the inlet to the outlet of the HTF loop. Parameters $\lambda_{P,1} - \lambda_{P,3}$ are identified for the inlet, midpanel, and outlet areas of the thermal transfer panel.

## V. Control-Criteria Metrics

This section discusses the control and performance metrics for the systematic control-criteria approach. The control-criteria metrics are used to set the acceptance criteria to accept or reject RTHS transfer system controllers and develop control design requirements.

### A. Control Metrics

The goal of the control metrics is to quantitatively evaluate the measured tracking performance of the control plant. The control metrics use scalar value representations based on the vector outputs of the numerical subsystem and control plant described in the previous sections. The setpoint temperature $T_{G,S}$ and interface feedback temperature $T_{G,F}$ introduced for tracking performance based on each subsystem interface temperature vector. Meanwhile, during an RTHS experiment, temperatures $T_{G,S}$ and $T_{G,F}$ are determined from the available measured states of the system. Three control metrics are defined as follows:

$$J_1 = \sqrt{\frac{\sum_{k=1}^{N} (T_{G,F}[k] - T_{G,S}[k])^2}{\sum_{k=1}^{N} (T_{G,S}[k])^2}} \tag{34}$$

$$J_2 = \frac{\sqrt{\sum_{k=1}^{N} (T_{G,F}[k] - T_{G,S}[k])^2 / N}}{\max |T_{G,S}|} \tag{35}$$

Downloaded by NASA LANGLEY RESEARCH CENTER on November 13, 2023 | http://arc.aiaa.org | DOI: 10.2514/1.J062857

$$J_3 = \frac{\max |T_{G,F} - T_{G,S}|}{\max |T_{G,S}|} \tag{36}$$

The control metrics are assessed by minimizing the values $J_1$, $J_2$, and $J_3$. The closer the control error indicator values are to 0, the better the controller performance. The first two control metrics are normalized root-mean-square error (NRMSE) measures, which assess the actual performance of the tracking controller. Control metric $J_1$ is the NRMSE relative to $T_{G,S}$ at each time step, while the maximum absolute amplitude of $T_{G,S}$ normalizes $J_2$. The third control metric $J_3$ is the normalized peak absolute error (NPAE), which assesses the tracking amplitude errors.

### B. Performance Metrics

Performance metrics are established to assess how the control strategies and estimation methods impact the global RTHS performance. They evaluate the ability of the controllers to reduce simulation error with respect to a reference model and establish RTHS acceptance criteria. The performance metrics used are the following:

$$\boldsymbol{PM}_1 = \mathbf{1} - \frac{\sqrt{\sum_{k=1}^{N} (\boldsymbol{T}_{\text{part}}[k] - \boldsymbol{T}_{\text{ref}}[k])^2}}{\sqrt{\sum_{k=1}^{N} (\boldsymbol{T}_{\text{ref}}[k])^2}} \tag{37}$$

$$\boldsymbol{PM}_2 = \mathbf{1} - \left| \frac{\max(|\boldsymbol{T}_{\text{part}}|) - \max(|\boldsymbol{T}_{\text{ref}}|)}{\max(|\boldsymbol{T}_{\text{ref}}|)} \right| \tag{38}$$

$$\boldsymbol{PM}_3 = \mathbf{1} - \left| \frac{\sum_{k=1}^{N} (\boldsymbol{T}_{\text{part}}[k])^2 - \sum_{k=1}^{N} (\boldsymbol{T}_{\text{ref}}[k])^2}{\sum_{k=1}^{N} (\boldsymbol{T}_{\text{ref}}[k])^2} \right| \tag{39}$$

where subscripts $(\cdot)_{\text{ref}}$ and $(\cdot)_{\text{part}}$ denote reference and partitioned system, respectively.

The performance metrics for global RTHS would ideally have a value of one. The closer these values from the performance are to 1, the better the global RTHS performance. The first performance metric $\boldsymbol{PM}_1$ is the second norm or NRMSE that quantitatively assesses the difference between responses $\boldsymbol{T}_{\text{ref}}$ and $\boldsymbol{T}_{\text{part}}$. The latter two performance metrics, $\boldsymbol{PM}_2$ and $\boldsymbol{PM}_3$, assess the amplitude errors between the reference and partitioned results. The indicator $\boldsymbol{PM}_2$ is the normalized maximum amplitude error (NMAE), and indicator $\boldsymbol{PM}_3$ is the normalized energy error (NEE) to assess the continuity of the heat flux at the interface.

For comparison, the performance metric vectors obtained with Eqs. (37–39) are combined to a scalar value $PM_i$ as

$$PM_i = \beta_{\text{mid}} \cdot \overline{\boldsymbol{PM}_{\text{mid}}} + \beta_{\text{edge}} \cdot \overline{\boldsymbol{PM}_{\text{edge}}} \tag{40}$$

where $\beta_{\text{mid}}$ and $\beta_{\text{edge}}$ are the weighting values given to the mean of the midpanel and edge-panel vectors, respectively. Because the thermal actuator is more effective in the midpanel region than at the edges, the weighting should be given a higher value at the midpanel area than at the edge.

## VI. Illustrative Example

This section demonstrates an illustrative example of thermomechanical RTHS for a lunar habitat. The example consists of a two-layered system where the numerical subsystem is lunar regolith, and the experimental subsystem is aluminum. The length and height of the system are 46.5 cm (18.30 in) and 21.3 cm (8.37 in), respectively. The thermal properties of the layer materials are provided in Table 1.

The physical components for the thermal actuator consist of 1) a Mydax CryoDax 16 recirculating cryogenic chiller model with a fluid temperature setpoint range from −70°C to +80°C; 2) a copper thermal transfer pipe system; and 3) a 3-mm-thick thermal transfer panel made of aluminum with a copper serpentine channel. The parameters for the thermal actuator models in this simulation were determined from prototype testing and observed experimental behavior in the laboratory. A set of step-input, open-loop experiments were performed to determine the parameters of each thermal actuator component model, listed in Table 2.

**Table 1 Illustrative example thermal material properties**

| Layer | Material | Height, $H$ [m] | Specific heat capacity, $C_p$ [J/(kg · K)] | Density, $\rho$ [kg/m$^3$] | Thermal conductivity, $k$ [W/(m · K)] |
|---|---|---|---|---|---|
| Top | Lunar regolith | 0.200 | 1053 | 2000 | 0.014 |
| Bottom | Aluminum 6061 T6 | 0.013 | 896 | 2700 | 167 |

The control-criteria approach developed in Sec. II is followed in this illustrative example for the thermomechanical RTHS problem. For the control metrics development and verification phase, a set of 1000 Proportional-Integral-Derivative (PID) controllers was created by adjusting 10 values of each controller gain. The values for each controller gain are shown in Fig. 8a. The scalar values $T_{G,S}$ and $T_{G,F}$ for the controller are defined as the mean temperature of the midpanel nodes in the $\boldsymbol{T}_{\text{i,d}}$ and $\boldsymbol{T}_{\text{i,m}}$ vectors. The thermal transfer panel is more effective in the midpanel region than the edges. Thus, using the midpanel region states will provide a good assessment of the effectiveness of the controller.

Simulations of the thermomechanical control plant were performed with each controller. The input to the control plant, the temperature at the interface of the numerical lunar regolith layer, was defined as an exponential temperature drop from 20 to −10°C over 40 min. Likewise, the cooling flux input to the thermomechanical RTHS system is a low-frequency half-cycle sine pulse excitation with frequency $2 \times 10^{-4}$ Hz and an amplitude of 35 W, which results in a smooth exponential temperature drop over the range of interest temperature for a lunar habitat. The thermal conductivity for the experimental subsystem layer was multiplied by a factor of 0.001 to account for the thermal resistance due to the temperature-controlled laboratory environment (even with the use of insulation).

The control metrics were calculated for each of the 1000 simulations, and a threshold of 5% was set for all control metrics. Then, the gains of the controllers that passed the metric control threshold were extracted. Finally, the new controller set is compared to the initial controller set in Fig. 8a, and its distribution of the gains is shown in Fig. 8b. Noticeably the integral gain has localized more than the proportional or derivative gains based on purely tracking performance. Thus, an integral gain in the $2.5–25 \times 10^{-2}$ range provides control metrics equal to or less than 5%.

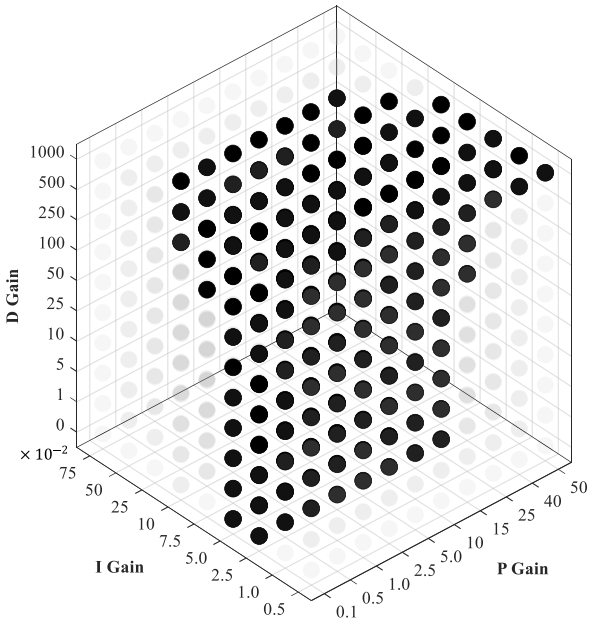
The new set of 255 PID controllers from the previous phase was used next for the performance metrics development and verification. First, an RTHS simulation was performed for each of the 255 controllers, starting from thermal equilibrium (all nodes at 20°C) and imposing a cooling load excitation to the numerical subsystem. The performance metrics defined in Eqs. (37–39) were computed and transformed through Eq. (40) to obtain all $PM_i$ values. The weighting values $\beta_{\text{mid}}$ and $\beta_{\text{edge}}$ were defined as 0.80 and 0.20, respectively. A threshold of 95% was set for all performance metrics, and every controller below these criteria was disregarded. Next, a new PID controller set with 184 controllers was extracted from the RTHS's performance results. The distribution of the new set of 184 PID controllers is shown in Fig. 8c, where the blue-filled dots denote the controllers that passed the performance threshold, and the unfilled dots denote the controllers that did not pass the criteria. Again, the controller gain distribution was narrowed down for the $I$ gains to the $2.5–10 \times 10^{-2}$ range.

The new set containing 184 PID controllers was then used in the return path to extract the associated control metrics values in the control requirements generation phase. The control requirements in this illustrative example were defined based on the mean control metric $J_i$ values of the controller set: $J_1 \leq 2.0$, $J_2 \leq 1.5$, and $J_3 \leq 3.0$. The $I$ gain range was further narrowed to $2.5–5.0 \times 10^{-2}$, while the $P$ gain range narrowed to 0.1–25. The $D$ gain distribution remained the same for all combinations.

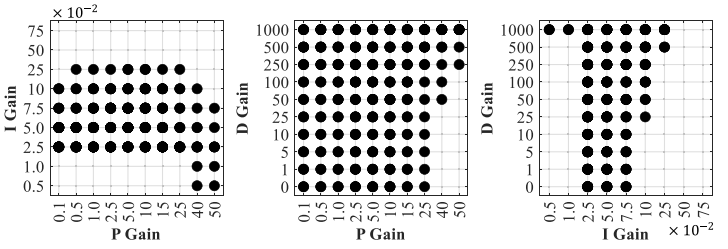
Downloaded by NASA LANGLEY RESEARCH CENTER on November 13, 2023 | http://arc.aiaa.org | DOI: 10.2514/1.J062857

**Table 2 Thermal transfer actuator system parameters**

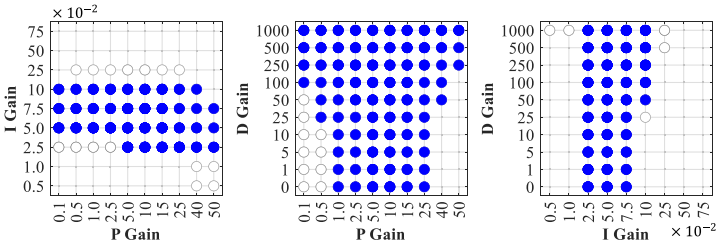
| Thermal actuator component | Parameter | Units | Value | Description |
|---|---|---|---|---|
| Heat Transfer Fluid (HTF) | $R_f$ | $K \cdot W^{-1}$ | $4 \times 10^{-4}$ | Thermal resistance |
| Cryogenic Chiller | $\dot{Q}_{C,\text{heat}}$ | W | 3000 | Heating exchange rate design capacity |
| | $Q_{C,\text{cool}}$ | W | 7200 | Cooling exchange rate design capacity |
| | $\epsilon_{\text{heat}}$ | — — | 0.0123 | Heating exchange effectiveness coefficient |
| | $\epsilon_{\text{cool}}$ | — — | 0.0300 | Cooling exchange effectiveness coefficient |
| | $e_{\text{tol}}$ | °C | 0.25 | Internal tracking error tolerance |
| Thermal Transfer Pipe System | $\lambda_{S,1}$ | 1/s | $9.3 \times 10^{-3}$ | State lumped parameter |
| | $\lambda_{S,2}$ | 1/s | $8.1 \times 10^{-3}$ | Input lumped parameter |
| | $\lambda_{S,3}$ | 1/s | $0.8 \times 10^{-3}$ | Disturbance lumped parameter |
| Thermal Transfer Panel | $\lambda_{P,1,\text{in}}$ | 1/s | $2.2 \times 10^{-2}$ | HTF inlet state lumped parameter |
| | $\lambda_{P,2,\text{in}}$ | 1/s | $1.7 \times 10^{-2}$ | HTF inlet input lumped parameter |
| | $\lambda_{P,3,\text{in}}$ | 1/s | $0.4 \times 10^{-2}$ | HTF inlet disturbance lumped parameter |
| | $\lambda_{P,1,\text{mid}}$ | 1/s | $2.2 \times 10^{-2}$ | HTF midpanel state lumped parameter |
| | $\lambda_{P,2,\text{mid}}$ | 1/s | $1.7 \times 10^{-2}$ | HTF midpanel input lumped parameter |
| | $\lambda_{P,3,\text{mid}}$ | 1/s | $0.6 \times 10^{-2}$ | HTF midpanel disturbance lumped parameter |
| | $\lambda_{P,1,\text{out}}$ | 1/s | $2.0 \times 10^{-2}$ | HTF outlet state lumped parameter |
| | $\lambda_{P,2,\text{out}}$ | 1/s | $1.4 \times 10^{-2}$ | HTF outlet input lumped parameter |
| | $\lambda_{P,3,\text{out}}$ | 1/s | $0.7 \times 10^{-2}$ | HTF outlet disturbance lumped parameter |
| | $\lambda_{P,4}$ | 1/s | $7.0 \times 10^{-4}$ | Contact heat loss state lumped parameter |
| | $\lambda_{P,5}$ | 1/s | $7.0 \times 10^{-4}$ | Contact heat loss input lumped parameter |
| | $w_{P,f}$ | — — | 0.7 | HTF loop weighting factor |
| | $w_{P,l}$ | — — | 0.3 | Contact heat loss weighting factor |



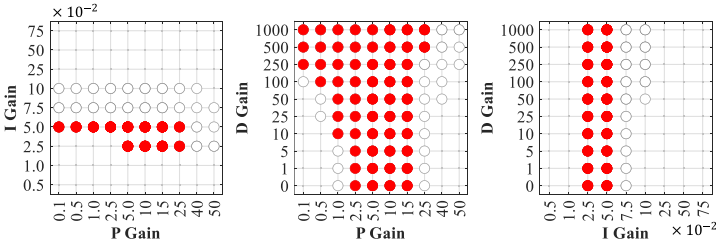

**a) PID controller set (black points – controller gains that have all control metrics ≤ 5%; faded points – controllers that did not pass the 5% control metric threshold)**




**b) PID controller set after control metrics assessment ($J_i \leq 5\%$) – 255 controllers**




**c) PID controller set after performance metric assessment ($PM_i \geq 95\%$) – 184 controllers**

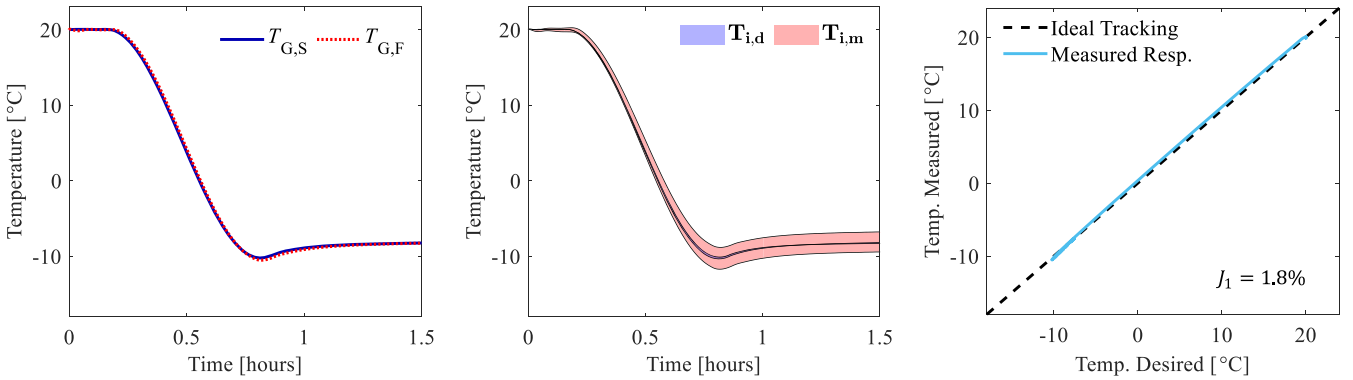



**d) Reduced PID controller set after control requirements – 86 controllers**

**Fig. 8 The set of PID controllers for the illustrative example.**

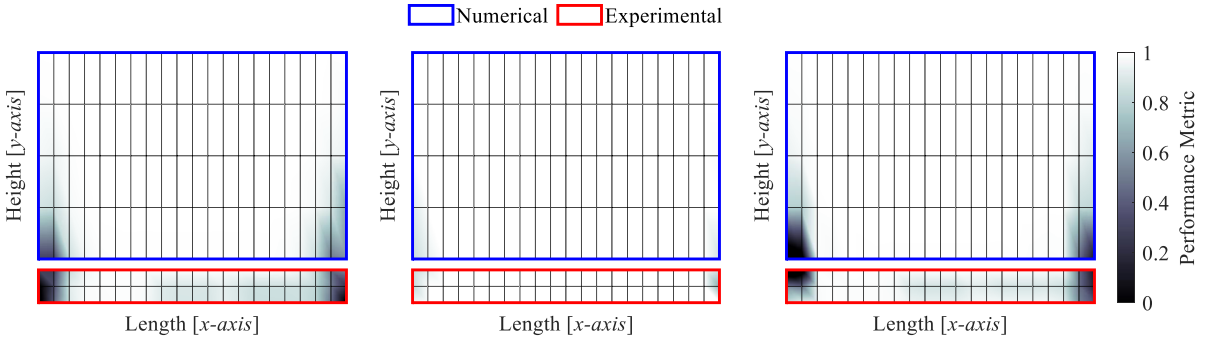
For the controller design phase, the defined control requirements threshold was used to extract the PID controller set that met the defined control metric criteria. A reduced set of 86 PID controllers was then selected, shown in Fig. 8d, where the red-filled dots denote the controllers that passed the control requirements. As a result, the optimal PID controller gains can be found in a smaller controller set that achieves all tracking control requirements and provides an RTHS performance exceeding 90%.

Downloaded by NASA LANGLEY RESEARCH CENTER on November 13, 2023 | http://arc.aiaa.org | DOI: 10.2514/1.J062857




**a) Tracking signals comparison** **b) Interface response distribution comparison** **c) Tracking performance of the chosen controller**

**Fig. 9 Tracking performance of the chosen PID controller.**




**a) $PM_1$ distribution** **b) $PM_2$ distribution** **c) $PM_3$ distribution**

**Fig. 10 Performance metric results of the chosen PID controller.**

One PID controller was chosen from the reduced controller set for future testing. The selected PID controller has the following gains: $P = 5, I = 0.025$, and $D = 10$. A controller with lower $P$ and $I$ gains was conservatively chosen to reduce overshoot or steady-state oscillation, as higher gains can increase these phenomena. The tracking performance results are shown in Fig. 9. The PID controller offers good tracking performance as seen with the scalar control signals in Figs. 9a and 9c, with a $J_1 = 1.8\%$. In Fig. 9b, the interface temperature distribution for the experimental subsystem is much wider when compared to the desired due to the thermal actuator. The wider distribution results from the thermal transfer panel having a nonuniform behavior within the localized effective area and the HTF loop having heat losses as it circulates above the experimental subsystem. The thermal distribution difference of the experimental subsystem with the desired temperature response does not exceed 1.5°C.

The performance metrics for the chosen controller are shown in Fig. 10. All performance metric distribution plots show lower values in the edges of the system due to the localized effectiveness of the thermal transfer panel at the center. In contrast, the edges of the experimental subsystem and the edges of the numerical interface show lower performance metrics. In this type of cooling load scenario where the absolute value of the initial temperature does not exceed other target temperature values, performance metrics $\boldsymbol{PM}_1$ and $\boldsymbol{PM}_3$ are more informative than $\boldsymbol{PM}_2$. However, $\boldsymbol{PM}_2$ is a good assessment metric for scenarios where the absolute value of a target temperature value exceeds the initial temperature.

Even though we are using the available temperature measurement for tracking control and temperature states to assess performance, it is important to replicate the thermal disturbance or thermal load effects on the structure or subsystem. Most importantly, we should evaluate if, through RTHS and the thermal transfer system, we can impose the thermal load on the experimental subsystem layer. As seen in Fig. 11a, the bottom layer experiences different temperatures through its thickness, meaning that energy flows through the system due to the imposed flux load from the top layer and the experimental heat flux.

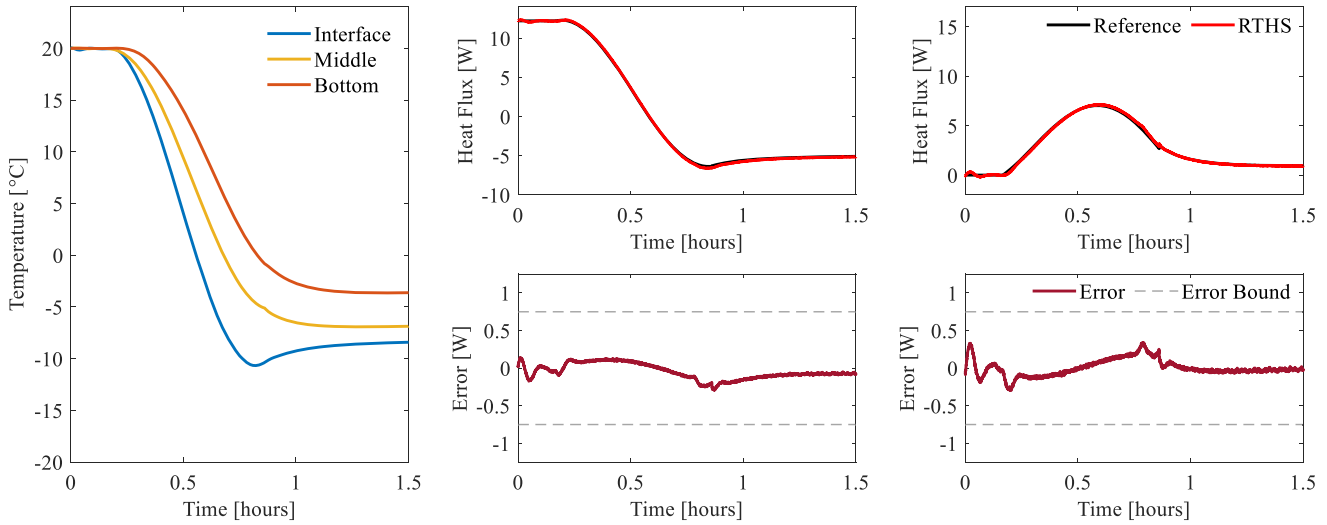
The reference and RTHS comparison for the mean imposed heat load from the top to the bottom layer and its respective error are plotted in Fig. 11b. These results demonstrate good RTHS performance imposing the cooling load on the bottom layer with an NMRSE = 1.1% and an error that does not exceed 0.5 W. We should also assess if the experimental feedback flux is in good agreement with the reference system. The results comparison and error for the feedback heat flux are shown in Fig. 11c. Again, the results indicate good agreement from the RTHS results with the reference, with an NMRSE = 2% and a time history error below 0.5 W.

The control and performance metric results provide guidance for the acceptance criteria that should be established for thermomechanical RTHS with cooling heat loads. We developed a set of acceptance criteria listed in Table 3 to reach a high level of performance with thermomechanical RTHS. The acceptance criteria address specifications that play a significant role in assuring the RTHS level of performance. These criteria should not be considered universal for all RTHS experiments but should be adapted for each specific application of RTHS based on the goals of the testing.

## VII. Conclusions

This study introduces a novel thermomechanical RTHS framework and problem formulation, expanding the range of hybrid simulation methods. The framework considers two-way coupling between the numerical and experimental subsystems for an innovative thermal transfer system design. Although the RTHS implementation in this paper is conceptual and computational, the models and parameters for the thermal transfer system components are based on experimental observations. Simultaneously, this conceptual study contributes to the development of RTHS theory by introducing a systematic approach for control and performance assessment and

Downloaded by NASA LANGLEY RESEARCH CENTER on November 13, 2023 | http://arc.aiaa.org | DOI: 10.2514/1.J062857




**a) RTHS experimental subsystem response** **b) Imposed heat flux comparison** **c) Feedback heat flux comparison**

**Fig. 11 Experimental response comparison to the reference system for the chosen PID controller.**

**Table 3 Thermomechanical RTHS acceptance criteria**

| Testing parameter | Requirement |
|---|---|
| Temperature measurement accuracy | $\pm 1°C$ |
| Laboratory thermal stability | $T_{amb} = 20 \pm 2°C$ |
| Effective area of the thermal transfer panel with respect to the experimental subsystem's total area | $A_{eff,p} \geq 0.70 A_{total,E}$ |
| Temperature distribution difference at the experimental interface | $\Delta \boldsymbol{T}_{i.m} \leq 2°C$ |
| Imposed thermal load error bounds | $\pm 0.75$ W $(J \cdot s^{-1})$ |
| Experimental feedback heat flux response error bound | $\pm 0.75$ W $(J \cdot s^{-1})$ |

defining requirements for implementing acceptance criteria to tackle and implement complex problems through RTHS. In addition, the result of acceptance testing will allow RTHS methods to reach higher performance levels and validate RTHS as a standard testing technique. One of the main contributions of this systematic approach is to serve as a model and set the path to determine further and define acceptance testing and criteria for RTHS applications.

The thermomechanical RTHS framework and a systematic control criteria approach are shown herein through a 2D heat conduction illustrative example of a lunar habitat. The cooling thermomechanical RTHS testing scope presented in this study can be expanded to further assess deep-space structures and deep-ocean or arctic systems.

## Acknowledgments

This work was supported by the Space Technology Research Institutes grant (no. 80NSSC19K1076) from NASA's Space Technology Research Grants Program.

## References

[1] Phillips, B. M., Takada, S., Spencer, B. F., Jr., and Fujino, Y., "Feedforward Actuator Controller Development Using the Backward-Difference Method for Real-Time Hybrid Simulation," *Smart Structures and Systems*, Vol. 14, No. 6, 2014, pp. 1081–1103. https://doi.org/10.12989/sss.2014.14.6.1081

[2] Friedman, A., Dyke, S. J., Phillips, B., Ahn, R., Dong, B., Chae, Y., Castaneda, N., Jiang, Z., Zhang, J., Cha, Y., Ozdagli, A. I., Spencer, B. F., Ricles, J., Christenson, R., Agrawal, A., and Sause, R., "Large-Scale Real-Time Hybrid Simulation for Evaluation of Advanced Damping System Performance," *Journal of Structural Engineering*, Vol. 141, No. 6, 2015, pp. 1–13. https://doi.org/10.1061/(ASCE)ST.1943-541X.0001093

[3] Gomez, D., Dyke, S., and Maghareh, A., "Enabling Role of Hybrid Simulation Across NEES in Advancing Earthquake Engineering," *Smart Structures and Systems*, Vol. 15, No. 3, 2015, pp. 913–929. https://doi.org/10.12989/sss.2015.15.3.913

[4] Fermandois, G. A., and Spencer, B. F., "Model-Based Framework for Multi-Axial Real-Time Hybrid Simulation Testing," *Earthquake Engineering and Engineering Vibration*, Vol. 16, No. 4, 2017, pp. 671–691. https://doi.org/10.1007/s11803-017-0407-8

[5] Silva, C. E., Gomez, D., Maghareh, A., Dyke, S. J., and Spencer, B. F., "Benchmark Control Problem for Real-Time Hybrid Simulation," *Mechanical Systems and Signal Processing*, Vol. 135, Jan. 2020, Paper 106381, https://linkinghub.elsevier.com/retrieve/pii/S0888327019306028. https://doi.org/10.1016/j.ymssp.2019.106381

[6] Najafi, A., Fermandois, G. A., Dyke, S. J., and Spencer, B. F., "Hybrid Simulation with Multiple Actuators: A State-of-the-Art Review," *Engineering Structures*, Vol. 276, Feb. 2023, Paper 115284, https://linkinghub.elsevier.com/retrieve/pii/S0141029622013608. https://doi.org/10.1016/j.engstruct.2022.115284

[7] Carrion, J. E., Spencer, B. F., and Phillips, B. M., "Real-Time Hybrid Simulation for Structural Control Performance Assessment," *Earthquake Engineering and Engineering Vibration*, Vol. 8, Dec. 2009, pp. 481–492. https://doi.org/10.1007/s11803-009-9122-4

[8] Börner, T., and Alam, M. R., "Real Time Hybrid Modeling for Ocean Wave Energy Converters," *Renewable and Sustainable Energy Reviews*, Vol. 43, March 2015, pp. 784–795. https://doi.org/10.1016/j.rser.2014.11.063

[9] Wang, X., Kim, R. E., Kwon, O.-S., Yeo, I.-H., and Ahn, J.-K., "Continuous Real-Time Hybrid Simulation Method for Structures Subject to Fire," *Journal of Structural Engineering*, Vol. 145, No. 12, 2019, Paper 04019152. https://doi.org/10.1061/(ASCE)ST.1943-541X.0002436

[10] Wu, T., and Song, W., "Real-Time Aerodynamics Hybrid Simulation: Wind-Induced Effects on a Reduced-Scale Building Equipped with Full-Scale Dampers," *Journal of Wind Engineering and Industrial Aerodynamics*, Vol. 190, July 2019, pp. 1–9. https://doi.org/10.1016/j.jweia.2019.04.005

[11] Al-Subaihawi, S., Kolay, C., Marullo, T., Ricles, J. M., and Quiel, S. E., "Assessment of Wind-Induced Vibration Mitigation in a Tall Building with Damped Outriggers Using Real-Time Hybrid Simulations," *Engineering Structures*, Vol. 205, Feb. 2020, Paper 110044, https://linkinghub.elsevier.com/retrieve/pii/S0141029619308600. https://doi.org/10.1016/j.engstruct.2019.110044

[12] Song, W., Sun, C., Zuo, Y., Jahangiri, V., Lu, Y., and Han, Q., "Conceptual Study of a Real-Time Hybrid Simulation Framework for Monopile Offshore Wind Turbines Under Wind and Wave Loads," *Frontiers in Built Environment*, Vol. 6, Aug. 2020, pp. 1–20. https://doi.org/10.3389/fbuil.2020.00129

[13] Sauder, T., and Alterskjær, S. A., "Hydrodynamic Testing of Wind-Assisted Cargo Ships Using a Cyber–Physical Method," *Ocean Engineering*, Vol. 243, Jan. 2022, Paper 110206, https://linkinghub.

Downloaded by NASA LANGLEY RESEARCH CENTER on November 13, 2023 | http://arc.aiaa.org | DOI: 10.2514/1.J062857

elsevier.com/retrieve/pii/S0029801821015213.
https://doi.org/10.1016/j.oceaneng.2021.110206

[14] Mostafaei, H., "Hybrid Fire Testing for Assessing Performance of Structures in Fire—Methodology," *Fire Safety Journal*, Vol. 58, May 2013, pp. 170–179, https://linkinghub.elsevier.com/retrieve/pii/S0379711213000386.
https://doi.org/10.1016/j.firesaf.2013.02.005

[15] Mostafaei, H., "Hybrid Fire Testing for Assessing Performance of Structures in Fire—Application," *Fire Safety Journal*, Vol. 56, Feb. 2013, pp. 30–38.
https://doi.org/10.1016/j.firesaf.2012.12.003

[16] Abbiati, G., Bursi, O. S., Stojadinovic, B., Tondini, N., and Whyte, C., "Hybrid Simulation of Heat Transfer Problems in Structural Applications—Coupled Problems 2015," *COUPLED PROBLEMS 2015—Proceedings of the 6th International Conference on Coupled Problems in Science and Engineering*, CIMNE, Barcelona, Spain, 2015, pp. 254–265, http://hdl.handle.net/2117/191131.

[17] Whyte, C. A., Mackie, K. R., and Stojadinovic, B., "Hybrid Simulation of Thermomechanical Structural Response," *Journal of Structural Engineering*, Vol. 142, No. 2, 2016, Paper 04015107.
https://doi.org/10.1061/(ASCE)ST.1943-541X.0001346

[18] "Hybrid Simulation for Multi-Hazard Engineering: A Research Agenda," Tech. Rept., MECHS, Zurich, Switzerland, March 2019, https://mechs.designsafe-ci.org/media/filer_public/af/fb/affb2d3d-c9ff-42cb-b09b-5cf36082f797/resagenda_year2_final.pdf.

[19] Najafi, A., Fermandois, G. A., and Spencer, B. F., "Decoupled Model-Based Real-Time Hybrid Simulation with Multi-Axial Load and Boundary Condition Boxes," *Engineering Structures*, Vol. 219, Sept. 2020, Paper 110868, https://linkinghub.elsevier.com/retrieve/pii/S0141029619344219.
https://doi.org/10.1016/j.engstruct.2020.110868

[20] Palacio-Betancur, A., and Gutierrez Soto, M., "Recent Advances in Computational Methodologies for Real-Time Hybrid Simulation of Engineering Structures," *Archives of Computational Methods in Engineering*, Vol. 30, April 2022, pp. 1637–1662.
https://doi.org/10.1007/s11831-022-09848-y

[21] Dyke, S. J., Marais, K., Bilionis, I., Werfel, J., and Malla, R., "Strategies for the Design and Operation of Resilient Extraterrestrial Habitats," *Sensors and Smart Structures Technologies for Civil, Mechanical, and Aerospace Systems 2021*, Vol. 1159105, edited by D. Zonta, H. Huang, and Z. Su, SPIE, Bellingham, WA, 2021, p. 2, https://www.spiedigitallibrary.org/conference-proceedings-of-spie/11591/2585118/Strategies-for-the-design-and-operation-of-resilient-extraterrestrial-habitats/10.1117/12.2585118.full.
https://doi.org/10.1117/12.2585118

[22] Maghareh, A., Lenjani, A., Krishnan, M., Dyke, S., and Bilionis, I., "Role of Cyber-Physical Testing in Developing Resilient Extraterrestrial Habitats," *Earth and Space 2021*, American Soc. of Civil Engineers, Reston, VA, 2021, pp. 1059–1068.
https://doi.org/10.1061/9780784483374.098

[23] Maghareh, A., Fu, Y., Montoya, H., Condori, J., Wang, Z., Dyke, S. J., and Montoya, A., "A Reflective Framework for Performance Management (REFORM) of Real-Time Hybrid Simulation," *Frontiers in Built Environment*, Vol. 6, Sept. 2020, pp. 1–13, https://www.frontiersin.org/article/10.3389/fbuil.2020.568742/full.
https://doi.org/10.3389/fbuil.2020.568742

[24] Maghareh, A., Dyke, S. J., Prakash, A., and Bunting, G. B., "Establishing a Predictive Performance Indicator for Real-Time Hybrid Simulation," *Earthquake Engineering and Structural Dynamics*, Vol. 43, No. 15, 2014, pp. 2299–2318.
https://doi.org/10.1002/eqe.2448

[25] Taler, J., and Ocłoń, P., *Finite Element Method in Steady-State and Transient Heat Conduction*, Springer, Dordrecht, The Netherlands, 2014, pp. 1604–1633.
https://doi.org/10.1007/978-94-007-2739-7_897

[26] Yadav, S., Dhillon, P., Kurtulus, O., Baxter, C., Ziviani, D., Horton, W. T., Karava, P., and Braun, J. E., "Design and Development of a Human Building Interaction Laboratory," *International High Performance Buildings Conference*, Purdue e-Pubs (by Purdue University Libraries), West Lafayette, IN, 2021, Paper 362. https://docs.lib.purdue.edu/ihpbc/362.

[27] Zhao, C., Sousa, A. C., and Jiang, F., "Minimization of Thermal Non-Uniformity in Lithium-Ion Battery Pack Cooled by Channeled Liquid Flow," *International Journal of Heat and Mass Transfer*, Vol. 129, Feb. 2019, pp. 660–670, https://linkinghub.elsevier.com/retrieve/pii/S0017931018331739.
https://doi.org/10.1016/j.ijheatmasstransfer.2018.10.017

[28] Mo, X., Zhi, H., Xiao, Y., Hua, H., and He, L., "Topology Optimization of Cooling Plates for Battery Thermal Management," *International Journal of Heat and Mass Transfer*, Vol. 178, Oct. 2021, Paper 121612.
https://doi.org/10.1016/j.ijheatmasstransfer.2021.121612

[29] Bendapudi, S., Braun, J. E., and Groll, E. A., "A Dynamic Model of a Vapor Compression Liquid Chiller," *International Refrigeration and Air Conditioning Conference*, Purdue e-Pubs (by Purdue University Libraries), West Lafayette, IN, 2002, p. 9, http://docs.lib.purdue.edu/iracc/568.

R. Ohayon
*Associate Editor*

Downloaded by NASA LANGLEY RESEARCH CENTER on November 13, 2023 | http://arc.aiaa.org | DOI: 10.2514/1.J062857